Renewable Energy 215 (2023) 118921

Contents lists available at ScienceDirect

Renewable Energy

journal homepage: www.elsevier.com/locate/renene

Evaluation and optimisation of hybrid sensible-latent heat thermal energy storage unit with natural stones to enhance heat transfer

Shuai Zhang, Yuying Yan *

Faculty of Engineering, University of Nottingham, University Park, Nottingham, UK

ARTICLE INFO

Keywords:
Phase change material/stones
Shell-and-tube
Heat transfer enhancement
Numerical simulation

ABSTRACT

Latent heat thermal energy storage improves the utilization efficiency of renewable energy. Phase change materials (PCMs) commonly suffer from low thermal conductivity and many heat transfer enhancement methods have been developed. However, conventional methods need additional material preparation and processing, which increases the cost and makes them less environmentally friendly. In the current study, natural stones are used to enhance the heat transfer of the PCM in a shell-and-tube unit, forming a hybrid sensible-latent heat storage configuration. Namely, stones, which are widely accessible, low-cost and environmentally friendly, not only act as sensible heat storage media but as the thermal enhancer of the PCM. Results indicate that the energy storage rate of cases with 25 mm-sized stones increased by 8.3%–92.6%. The case with a filling height of 72.8 mm is superior owing to the high energy storage rate and large total stored energy. The stone size rarely influences the total stored energy that increases almost linearly with the void fraction, while it affects the energy storage rate significantly. Cases with 20 mm and 40 mm-sized stones generally have a higher storage rate. Finally, the mechanism is analysed.

1. Introduction

Thermal energy storage (TES) addresses the temporal and geographical mismatch between energy supply and demand, improving the utilization efficiency of renewable energy [1–4]. Moreover, this technology can store unstable thermal energy but release stable thermal energy, which overcomes the instability of some renewable energy resources [5–8]. Sensible heat storage materials (SHMs) such as stones are widely accessible and low-cost [9,10], and their thermal conductivity is relatively high (e.g. granite: 1.73–3.98 W/(m·K)) [11]. Latent heat storage materials (or phase change materials, PCMs) are more attractive because their energy density is large, and the temperature during charging and discharging keeps almost constant [12,13]. However, the thermal conductivity of most PCMs is low [14–16]. For example, the thermal conductivity of paraffin is only 0.1–0.3 W/(m·K) [17], which leads to the slow storage rate of renewable energy.

Some technologies have been developed to enhance the heat transfer of the PCM. There are generally four heat transfer enhancement structures for the shell-and-tube heat storage units: porous skeletons, fins, nanoparticles, and heat pipes. In terms of the porous skeleton, Liu et al. [18] studied the melting of the copper foam-enhanced paraffin in a horizontal shell-and-tube unit. Buonomo et al. [19] investigated the performance of aluminium foam partially filled in a heat storage unit. The results indicate that the melting time of the PCM is reduced as the thickness of the metal foam increases. Zhang & Yan [20] studied the energy release performance of molten salt enhanced by ceramic foam, where the position and filling height of the ceramic foam were optimised. They found that the upper-filled foam was superior to the lower-filled foam, and the solidification time of molten salt can be shortened by 52%. Additionally, the energy release rate of the unit filled with ceramic foam was increased by 118%, and the ceramic showed good corrosion resistance to molten salt.

Concerning fins, Yang et al. [21] performed a numerical simulation to study the melting process of paraffin enhanced by annular fins in a heat storage unit, where the influence of the number, height and thickness of fins was analysed. Huang & Liu [22] developed tree-shaped fins to enhance the heat transfer of the PCM and found that the novel fins shortened the total melting and solidification time by 35% and 49%, respectively. The effect of natural convection is significant in the melting process, while it is negligible in the solidification process. The upward flow of heat transfer fluid (HTF) improves the melting of the PCM, while the downward flow of the HTF is superior for solidification. Dekhil et al.

* Corresponding author.
E-mail address: Yuying.Yan@nottingham.ac.uk (Y. Yan).

https://doi.org/10.1016/j.renene.2023.118921
Received 10 January 2023; Received in revised form 30 May 2023; Accepted 13 June 2023
Available online 14 June 2023

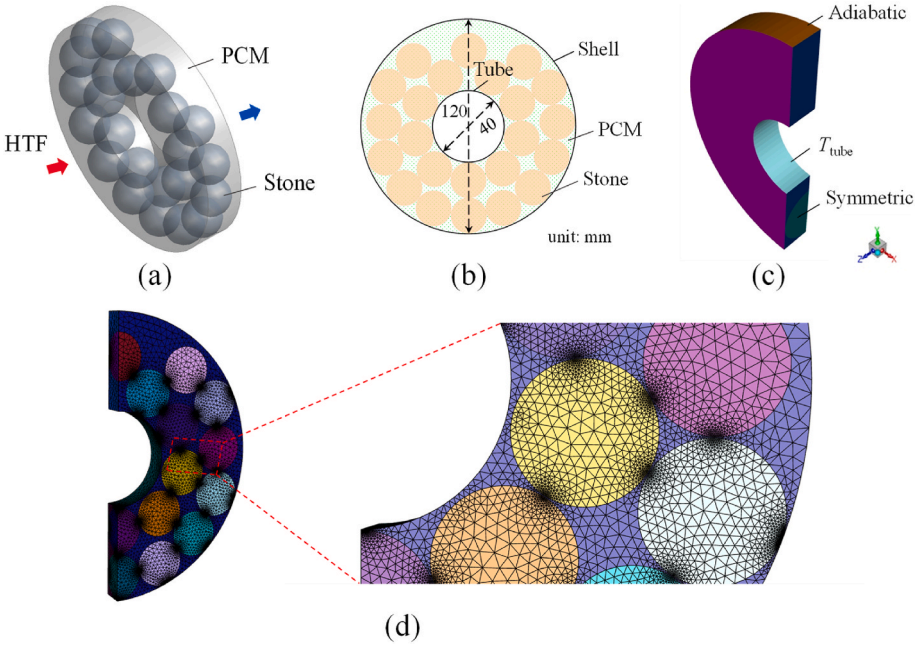

Fig. 1. (a) Schematic of the hybrid sensible-latent heat storage unit; (b) cross-section of the heat storage unit; (c) physical model used in the current simulation; (d) mesh of the computational domain.

Table 1
Detailed information on stones in the current simulation.

d, mm	N	*H*, mm	*d*, mm	N	*H*, mm	*d*, mm	N	*H*, mm
20	1	20.0	25	1	25.0	30	1	30.0
	5	35.4		3	31.6		3	40.0
	8	46.0		5	49.5		5	65.6
	12	62.9		7	72.8		7	92.3
	16	82.7		9	96.3		8	110.0
	20	97.0		12	119.3			
	23	112.0						
35	1	35.0	40	1	40.0			
	3	49.4		3	60.0			
	5	82.9		5	100.0			
	7	109.5		6	120.0			

**d*: diameter of stones; *N*: number of stones in a single unit; *H*: filling height.

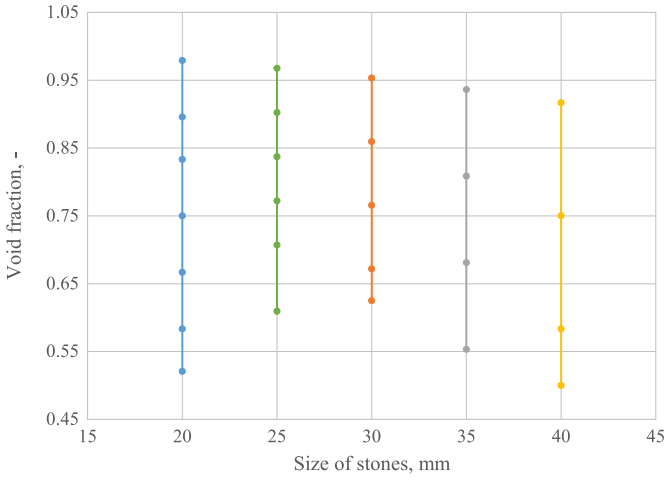

Fig. 2. Void fraction of all simulation cases.

Table 2
Properties of granite and paraffin [11,17].

Property	Granite	Paraffin
Density, kg/m^3	2640	785
Specific heat, J/(kg·K)	820	2850
Thermal conductivity, W/(m·K)	2.86	0.3 (solid)/0.1 (liquid)
Melting point, °C	–	54.4–64.1
Latent heat, J/kg	–	175,240
Viscosity, mPa·s	–	3.65
Coefficient of thermal expansion, K^{-1}	–	3.085×10^{-4}

[23] studied the effect of longitudinal and radial fins. Longitudinal fins show better heat transfer enhancement performance than radial fins. The melting fraction in the longitudinal fin configuration is 50% in 2 h, while that in the radial fin configuration is 44%. The solidification fraction in the longitudinal fin configuration is 50% in 2 h, while that in the radial fin configuration is 43%.

For nanoparticles, Mahdi et al. [24] studied alumina nanoparticles in multiple PCMs for thermal energy storage. Their results indicate that the solidification rate can be increased by 19%. However, Parsazadeh & Duan's study suggests that adding nanoparticles results in a longer charging time and lower energy storage rate [25].

Another heat transfer enhancement method is using heat pipes. Shabgard et al. [26] analysed the influence of heat pipes on thermal energy storage for solar power generation, where KNO_3 and Therminol VP-1 were used as the PCM and HTF, respectively. In Module 1, the HTF flows through the inner tube, while PCM surrounds that; the orientation of heat pipes has little effect on the thermal response. In Module 2, HTF flows over the tube, while PCM is contained within that; the orientation of heat pipes plays a significant role in the thermal response. Nithyanandam & Pitchumani [27] adopted similar modules and studied the impact of the number of heat pipes. They found that Module 1 stored more thermal energy, and the one with four heat pipes had the best performance.

Although many methods have been developed to enhance the heat transfer of the PCM, they commonly need additional material preparation and processing, which consumes water and electricity and emits greenhouse gas, making them less environmentally friendly. Natural

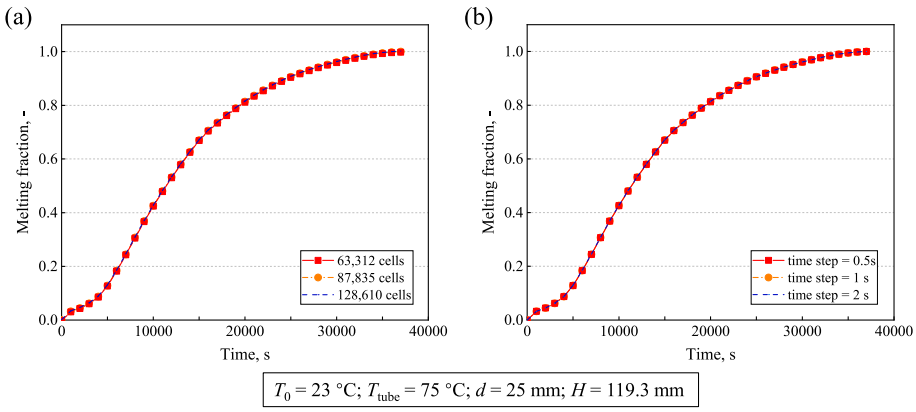

Fig. 3. Independence test of (a) grid and (b) time step.

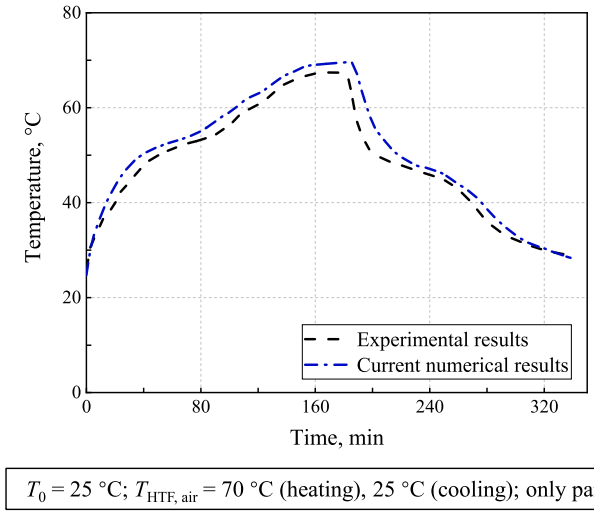

Fig. 4. Verification of the Melting/Solidification model with Atal et al. [40]'s experimental data.

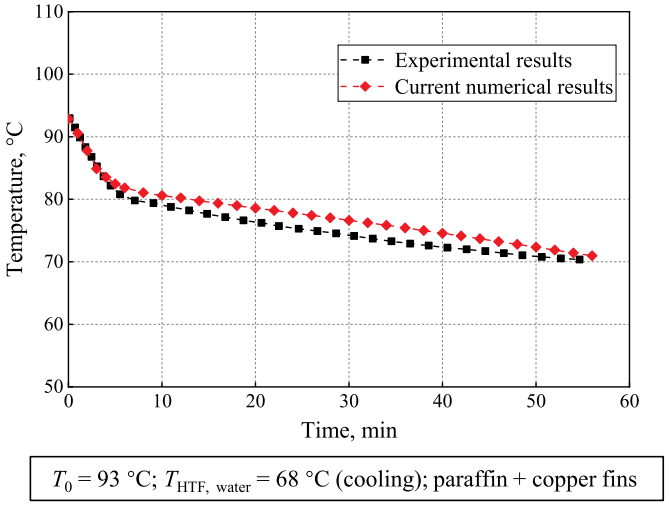

Fig. 5. Model verification with Al-Abidi et al. [41]'s experimental data.

stones have higher thermal conductivity; more importantly, they are naturally and widely accessible, so they are environmentally friendly and low-cost. However, the stone/PCM heat storage structure is rarely studied, which leads to a poor understanding of this configuration and hampers its potential applications. In the current research, natural stones are used to enhance the heat transfer of the PCM; meanwhile, they act as sensible heat storage media, forming a hybrid sensible-latent heat storage configuration. A numerical simulation is performed, and the energy storage performance in a shell-and-tube unit is evaluated. The melting front, velocity field, temperature response, and energy storage performance are analysed. Additionally, the configuration of stones is optimised to get superior structures. This study aims to guide the potential application of high-performance, low-cost, and environmentally friendly thermal energy storage technology.

2. Mathematical model

2.1. Description of hybrid energy storage unit

The schematic of the hybrid sensible-latent heat storage unit is shown in Fig. 1(a). The PCM and natural stones fill the annular space between the shell and the inner tube. The PCM acts as the latent heat storage medium, while natural stones act as the sensible heat storage medium, forming a hybrid sensible-latent heat storage configuration. Natural stones also act as the thermal enhancer of the PCM because their thermal conductivity is much larger than that of the PCM.

In practice, the shape of natural stones is irregular, making it difficult to evaluate the effect of various parameters such as size and height. It is assumed that stones are spherical to assess various parameters and identify regularities.

Spherical stones are arranged tangent to each other in a shell-and-tube unit with an inner diameter of 40 mm and an outer diameter of 120 mm (Fig. 1(b)). Actually, there are several different arrangements of stones. The current arrangement considers gravity and makes the stones be in contact with the tube as far as possible in order to conduct the heat of the tube.

Different sizes and heights of stones are considered to get superior structures. Detailed information on stones is listed in Table 1. Taking d (diameter of stones) = 20 mm as the example, the length of the single unit is 20 mm; the maximum N (number of stones) is 23 (the complete filling), while the minimum is 1. H (filling height) is measured using the Auto CAD package; for instance, there are five 20 mm-sized stones; in that case, the stone array is measured to be 35.4 mm high, so H is 35.4 mm. The void fraction is the ratio of the void volume to the total volume and is calculated by:

$$\varepsilon = \frac{V_{void}}{V_{total}} = \frac{V_{total} - V_{stone}}{V_{total}} = 1 - \frac{\frac{\pi d^3}{6} N}{\frac{\pi\left(D_{shell}{}^2 - D_{tube}{}^2\right)}{4} l_u} \quad (1)$$

where ε is the void fraction; V_{void}, V_{stone}, and V_{total} are the void, stone, and total volumes, respectively; D_{shell} and D_{tube} are the shell and tube diameters, respectively; l_u is the length of a single unit, which equals d.

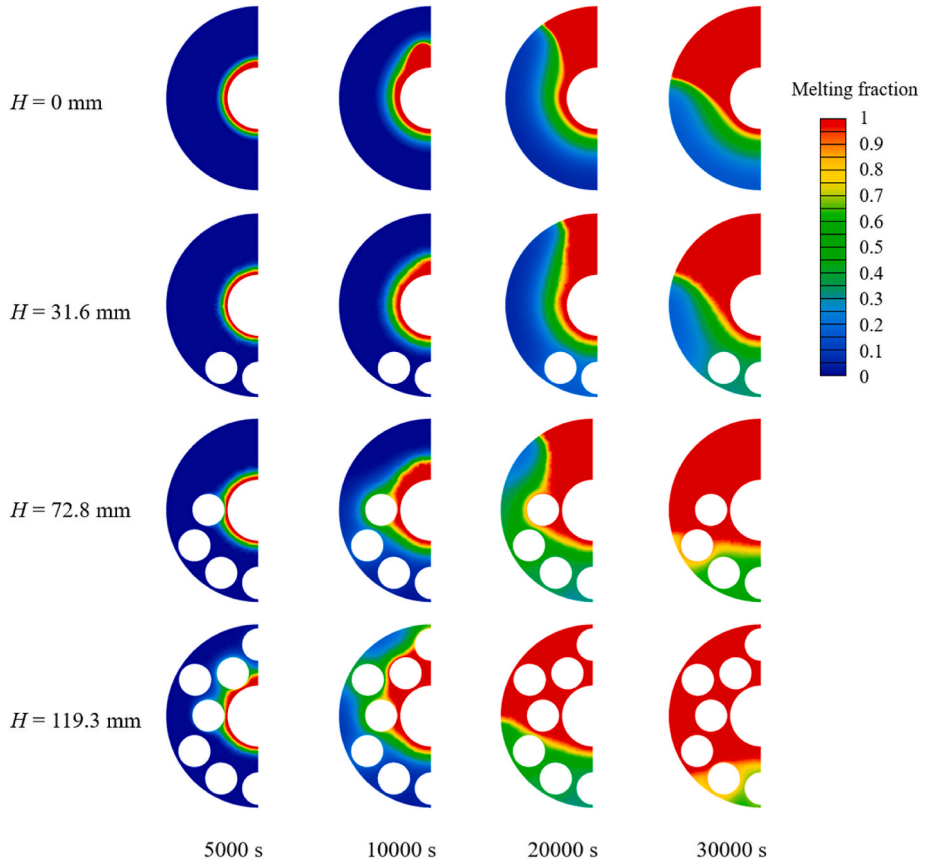

Fig. 6. Melting front of phase change material at different time (the plane at half the thickness).

The void fraction of all simulation cases, which ranges from 0.50 to 0.98, is presented in Fig. 2.

Due to symmetry, only a quarter of a single unit is used as the computational domain (Fig. 1(c)). The extremely small gap between two tangent spheres would lead to high skewness, which easily causes computational divergence. A common approach to this problem is to reduce the size of the sphere to 0.99 times (the "near-miss" model) [28], which is adopted in the current study. The mesh between neighbouring spheres is refined by reducing size. For the interior of spheres, large meshes with ~2 mm are created to save the computational source (Fig. 1 (d)). For the gap between two neighbouring spheres, small meshes with ~0.2 mm are created to improve the computational accuracy. The maximum skewness of the volume mesh is 0.78, which meets the requirement of the fluid simulation [29].

2.2. Governing equations

Some assumptions are made for the numerical simulation: (1) the PCM and stones are isotropic and homogenous; (2) the properties of energy storage materials, except for the density of the liquid PCM, are constant; (3) the liquid PCM is incompressible; (4) the Boussinesq approximation is employed to deal with natural convection. Assumptions (1)–(4) are usually used in simulating the melting of the PCM and have been adopted in numerous studies such as Refs. [30–34]. The density of the liquid PCM is assumed to vary linearly with temperature in Boussinesq approximation; so, the natural-convection problem is simplified, and the convergence can be got faster [35,36].

The continuity equation is:

$$\nabla \bullet \vec{U} = 0 \tag{2}$$

The momentum equations are as follows:

$$\rho_{\mathrm{PCM}}\frac{\partial u}{\partial t}+\rho_{\mathrm{PCM}}\left(\vec{U}\bullet\nabla u\right)=-\frac{\partial p}{\partial x}+\mu_{\mathrm{PCM}}\nabla^2 u-\frac{(1-\varphi)^2}{(\varphi^3+\omega)}A_{\mathrm{mushy}}u \tag{3}$$

$$\rho_{\mathrm{PCM}}\frac{\partial v}{\partial t}+\rho_{\mathrm{PCM}}\left(\vec{U}\bullet\nabla v\right)=-\frac{\partial p}{\partial y}+\mu_{\mathrm{PCM}}\nabla^2 v+\rho_{\mathrm{PCM}}\,g\,\beta\left(T-T_{\mathrm{m,s}}\right)-\frac{(1-\varphi)^2}{(\varphi^3+\omega)}A_{\mathrm{mushy}}v \tag{4}$$

$$\rho_{\mathrm{PCM}}\frac{\partial w}{\partial t}+\rho_{\mathrm{PCM}}\left(\vec{U}\bullet\nabla w\right)=-\frac{\partial p}{\partial z}+\mu_{\mathrm{PCM}}\nabla^2 w-\frac{(1-\varphi)^2}{(\varphi^3+\omega)}A_{\mathrm{mushy}}w \tag{5}$$

where U (u, v, and w are the components of the velocity vector in x, y, and z directions, respectively) is the fluid velocity [37]; ρ is the density. t is the time, which is transient; thus, the dynamic energy storage process can be simulated. p is the pressure; T is the temperature; g is the gravitational acceleration. μ and β are the viscosity and the thermal expansion coefficient respectively; A_{mushy} is the mushy zone constant; $T_{\mathrm{m,\,s}}$ is the solidus temperature of the PCM [38]. ω is a small number (0.001) to avoid being divided by zero. φ is the melting fraction in a single cell, which is evaluated by the enthalpy method [39]:

$$\varphi=\begin{cases}0 & T<T_{\mathrm{m,s}}\\ \dfrac{T-T_{\mathrm{m,s}}}{T_{\mathrm{m,l}}-T_{\mathrm{m,s}}} & T_{\mathrm{m,s}}\le T\le T_{\mathrm{m,l}}\\ 1 & T>T_{\mathrm{m,l}}\end{cases} \tag{6}$$

where $T_{\mathrm{m,\,l}}$ is the liquidus temperature of PCM.

The energy equation is given by Ref. [39]:

$$\rho_{\mathrm{PCM}}c_{\mathrm{p,PCM}}\left(\frac{\partial T}{\partial t}+\vec{U}\bullet\nabla T\right)=k_{\mathrm{PCM}}\nabla^2 T-\rho_{\mathrm{PCM}}L\frac{d\varphi}{dt} \tag{7}$$

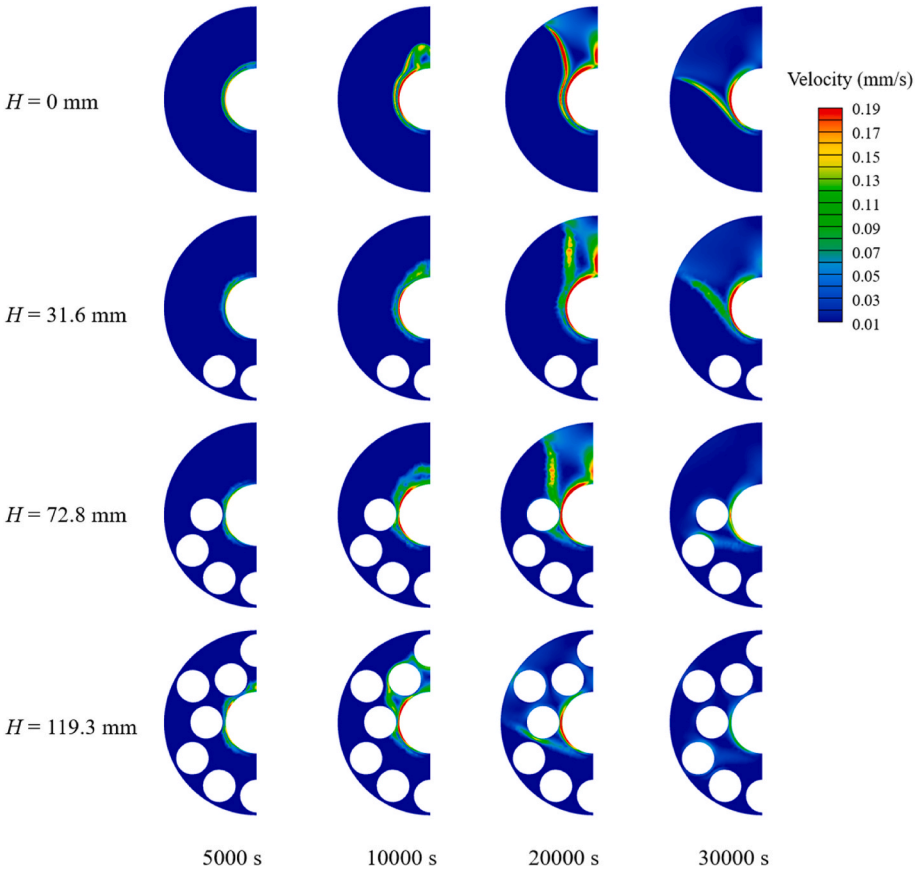

Fig. 7. Velocity distribution of phase change material at different time (the plane at half the thickness).

where c_p is the specific heat; L is the latent heat; k is the thermal conductivity.

Paraffin is used as the PCM, and the type of stone is granite. Their thermo-physical properties are listed in Table 2.

2.3. Initial and boundary conditions

The initial temperature of the whole computational domain is 23 °C:

$$T_0 = 23°C \tag{8}$$

The temperate of the inner tube is set as 75 °C:

$$T_{tube} = 75°C \tag{9}$$

The shell is assumed to be adiabatic:

$$\frac{\partial T_{shell}}{\partial x} = 0, \frac{\partial T_{shell}}{\partial y} = 0, \frac{\partial T_{shell}}{\partial z} = 0 \tag{10}$$

At the interface between the PCM and stones:

$$T_{PCM} = T_{stone} \tag{11}$$

$$(-k_{PCM}\nabla T_{PCM}) \bullet \boldsymbol{n} = (-k_{stone}\nabla T_{stone}) \bullet \boldsymbol{n} \tag{12}$$

where $\boldsymbol{n}$ is the unit normal vector to the interface between the PCM and stones [37].The initial and boundary conditions remain constant.

2.4. Independence test of grid and time step

The numerical model is solved using ANSYS Fluent. The governing equations are differentiated using the finite volume method (FVM) and solved simultaneously. The pressure and velocity are coupled using the SIMPLE scheme, and the pressure, momentum, and energy terms are discretised using the second-order upwind method. The under-relaxation factors are set as 0.3, 1, 1, 0.7, 0.9, and 1 for pressure, density, body forces, momentum, liquid fraction update, and energy, respectively. The convergence criteria for continuity, momentum, and energy equations are 10^{-4}, 10^{-4}, and 10^{-6}, respectively. The independence test of the grid and time step is carried out. First, three mesh sets (63,312 cells, 87,835 cells and 128,610 cells) are tested at the case of d = 25 mm and H = 119.3 mm. It is seen from Fig. 3(a) that there is little difference in melting fraction between the three mesh sets. Then, time steps of 0.5 s, 1 s and 2 s are tested, and the difference in total melting time is less than 0.3%. Thus, the mesh set of 87,835 cells and the time step of 1 s are employed in the current simulation.

2.5. Model verification

The numerical model is verified from two aspects. First, the Melting/Solidification model is verified. Atal et al. [40] studied the melting and solidification of paraffin in a horizontal heat storage unit and measured the temperature at the midpoint between the inner and outer tubes. Fig. 4 indicates that the overall trend of the numerical results is consistent with the experimental data. The difference should be attributed to the fact that: in Atal et al.'s experiment, there is no insulation at one end of the tube, so heat loss exists; by contrast, the boundary is set as adiabatic in the simulation. At the end of melting, the difference between the numerical and experimental data is 2.2 °C (3.3%); then, the difference gets smaller. At the end of solidification, the numerical results are almost identical to the experimental results. Therefore, the Melting/Solidification model is validated.

Second, the stone/PCM configuration is verified. However, since the stone/PCM configuration is a novel structure, there is little experimental data in the open literature. The principle of this configuration is that the thermal enhancer increases the heating area of the PCM. The finned unit

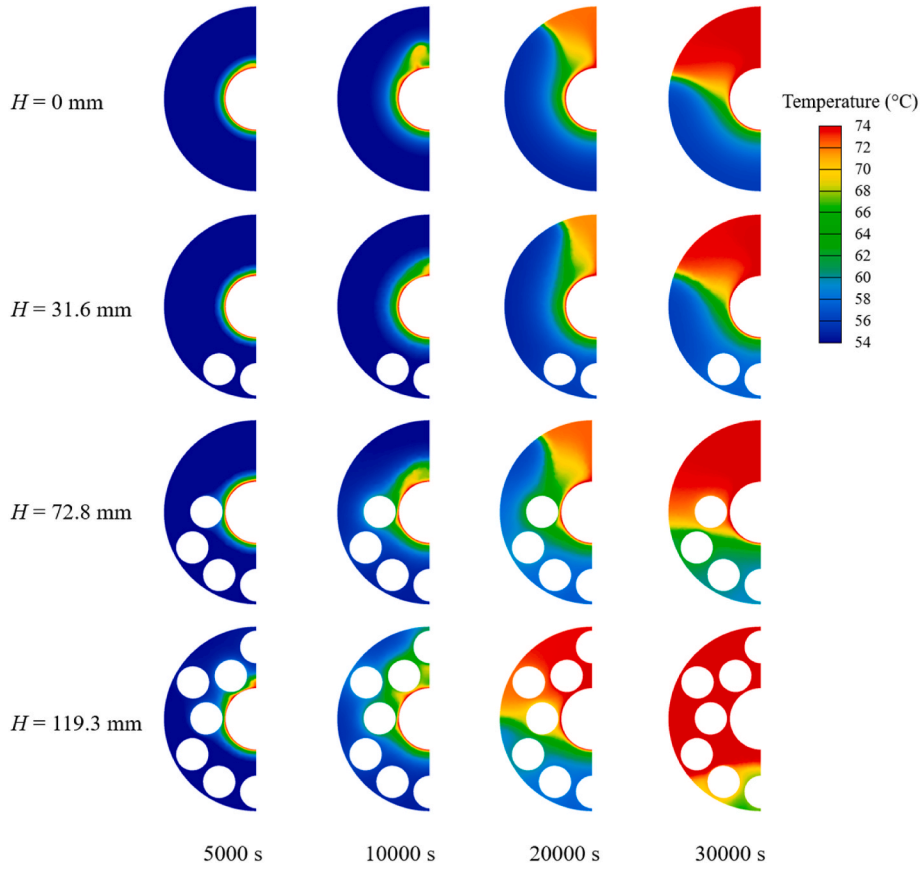

Fig. 8. Temperature field of phase change material at different time (the plane at half the thickness).

has the same principle; thus, the experimental results of this structure are used to validate the model. Al-Abidi et al. [41] investigated the solidification of paraffin in a finned heat storage unit. The comparison between the recorded temperature and numerical results is shown in Fig. 5, and the maximum difference is less than 5%. Therefore, the current numerical model is validated.

3. Results and discussions

3.1. Performance analysis

Taking cases of $d = 25$ mm as an example, the thermal energy storage performance is analysed, and the melting front of the PCM is shown in Fig. 6. The selected plane is at half the thickness, i.e. $z = 6.25$ mm (z means the z direction and is marked in Fig. 1(c); the total thickness of the computation domain of these cases is 12.5 mm). It is seen that at 5000 s, the PCM surrounding the tube is melted first. The mushy zone in the case of $H = 119.3$ mm is a little larger, while there is no significant difference between the other three cases. At 10,000 s, the mushy zone in cases of $H = 72.8$ mm and $H = 119.3$ mm is larger than the other two cases. This is because some stones are in contact with the inner tube, which helps transfer the tube's heat to the PCM, so the PCM around these stones is melted faster. Due to natural convection, the melting rate at the upper half is significantly higher than that of the lower half. At 30,000 s, the PCM at the upper half in cases of $H = 72.8$ mm and $H = 119.3$ mm is all melted; by contrast, there is still some mushy PCM in the cases of $H = 0$ mm and $H = 31.6$ mm. It is noted that the melting front of these two cases is almost identical from 5000 s to 30,000 s. That should be attributed to the fact that stones are placed at the bottom of the annular space and are not in contact with the inner tube, so the effect on the melting front is insignificant from 5000 s to 30,000 s.

Fig. 7 shows the velocity distribution of the PCM and suggests that for the case of $H = 0$ mm, the velocity at 5000 s is small owing to the limited flow space. As the melting proceeds, the flow space expands, and the liquid PCM is accelerated. And the velocity near the tube and at the solid/liquid interface is higher than that in other regions, which results from the natural convection. For the case of $H = 119.3$ mm, there is little difference in the velocity field compared to that of $H = 0$ mm at 5000 s. However, at 20,000 s (and 30,000 s), the difference in the flow space is significant (Fig. 6), which leads to the different velocity fields. Since stones restrict the flow of the liquid PCM, the velocity is smaller than that of $H = 0$ mm.

It is seen from Fig. 8 that the difference in the temperature fields between the four cases is insignificant at 5000 s. For the case of $H = 72.8$ mm, the PCM around the stone, which is in contact with the inner tube, has a slightly higher temperature at 10,000 s because the stone helps conduct the tube's heat to the PCM. A similar phenomenon can be observed in the case of $H = 119.3$ mm. Due to natural convection, the temperature at the upper half is higher than that at the lower half. At 30,000 s, the temperature difference between the upper and lower half is remarkable in the cases of $H = 0$ mm and $H = 31.6$ mm; by contrast, it is less significant in those of $H = 72.8$ mm and $H = 119.3$ mm.

The energy storage parameters of all cases are calculated based on a 40 mm-length unit for comparison, and the variation of the melting volume with time is plotted in Fig. 9(a). At the initial stage, the melting volume of the PCM in different cases is almost identical; afterwards, the melting volume in the case of $H = 119.3$ mm rises faster. However, at 20,000 s–30,000 s, the melting volume in the case of $H = 72.8$ mm is the largest. Fig. 9(b) shows the average melting rate and indicates that the melting rate in cases with stones is higher than without. The melting rate increases as the filling height increases from 25.0 mm to 72.8 mm. It is noted that the increase in the melting rate is more significant when the filling height increases from 49.5 mm to 72.8 mm because some stones are in contact with the inner tube (Fig. 10) and transfer the tube's heat to

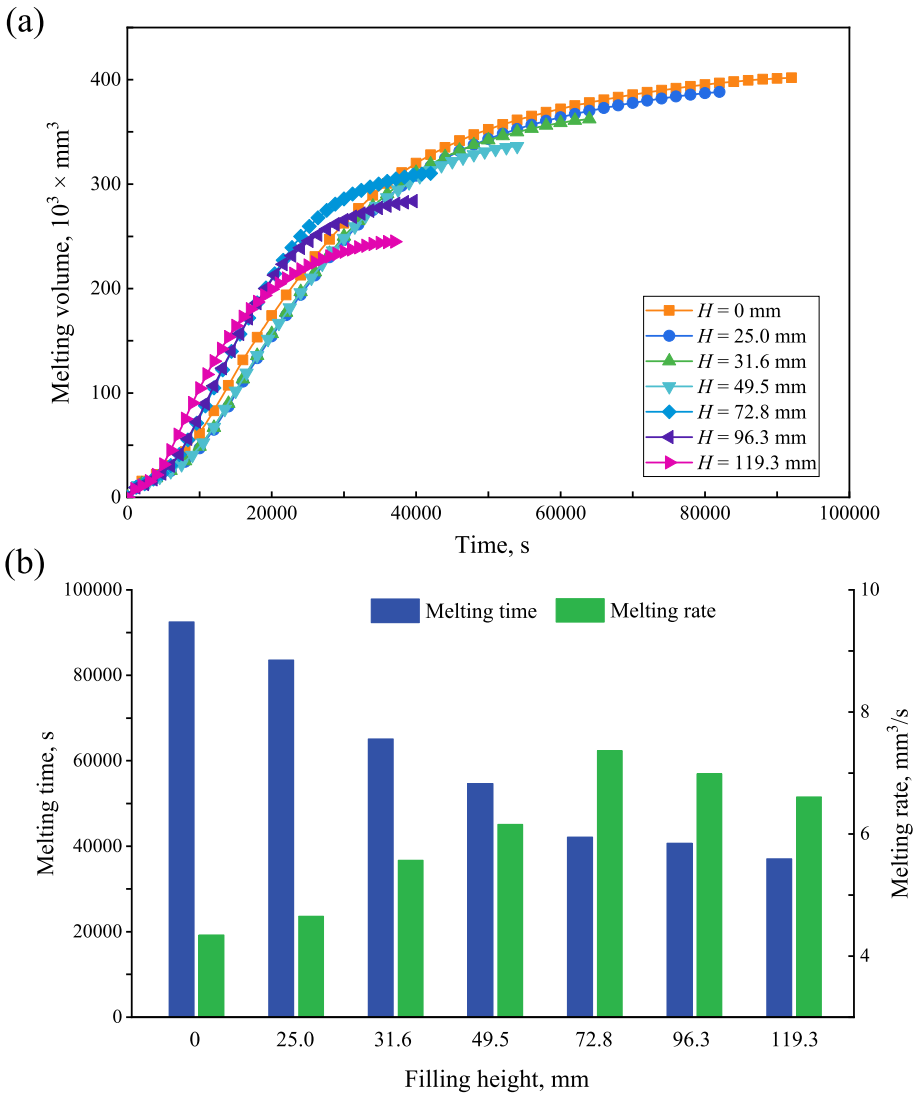

Fig. 9. (a) Variation of the melting volume of the PCM with time; (b) effect of the filling height of stones on melting time and rate.

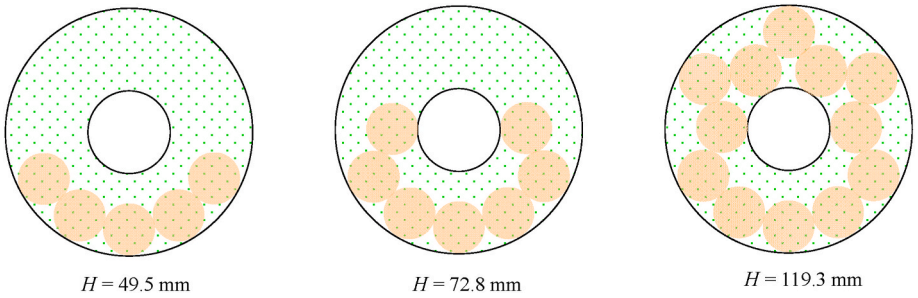

Fig. 10. Schematic of cases of H = 49.5 mm, 72.8 mm, and 119.3 mm.

the PCM. The melting rate in the case of H = 72.8 mm is the largest, which is 69.5% higher than without stones.

However, the melting rate decreases as the filling height further increases (72.8 mm–119.3 mm) because natural convection, which is strong at the top, is suppressed significantly by stones (Fig. 10).

Fig. 11 shows the variation of heat flux of the inner tube with time. The heat flux generally decreases with time because the temperature difference between the energy storage material and the inner tube decreases. Before 10,000 s, the heat flux in the case of H = 119.3 mm is the largest because the stone number is the most, and the heat transfer performance is the best. The heat flux in the cases of H = 72.8 mm and H = 96.3 mm is also high; however, it becomes smaller than that in the other four ones after about 25,000 s. As Fig. 8 shows, the temperature in the case of H = 72.8 mm is higher than that of H = 31.6 mm, which leads to a lower temperature difference between the energy storage material and the inner tube and, thus, a lower heat flux. The heat flux in the cases of H = 25.0 mm, H = 31.6 mm, and H = 49.5 mm is basically the same as that of H = 0 mm.

Temperature uniformity is another important characteristic of energy storage material. The average temperature, maximum temperature

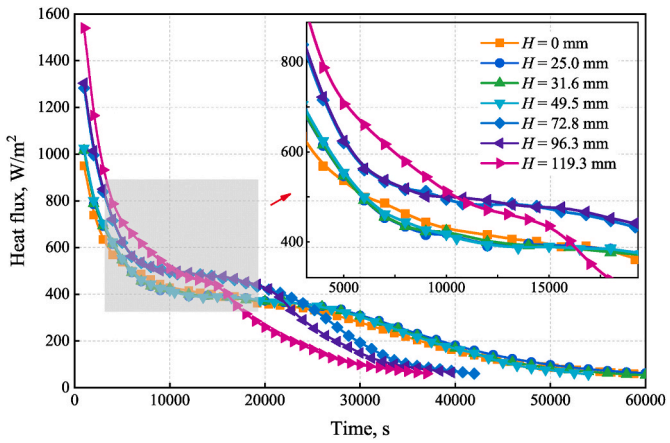

Fig. 11. Variation of heat flux of the inner tube with time in difference cases.

difference, and temperature non-uniformity index are shown in Fig. 12. The maximum temperature difference is calculated by:

$$\Delta T\ (f_l) = T_{max}(f_l) - T_{min}(f_l) \tag{13}$$

The temperature non-uniformity index is defined as:

$$\delta\ (f_l) = \sqrt{\frac{\sum_{i=1}^{n} [T_i(f_l) - \overline{T\ (f_l)}]^2}{n}} \tag{14}$$

where f_l is the average melting fraction; n is the number of cells; $T_i\ (f_l)$ is the temperature of cell i at f_l; $T_{max}(f_l)$ and $T_{min}(f_l)$ are the highest and lowest temperature of energy storage materials, respectively; $\overline{T(f_l)}$ is the average temperature of energy storage materials.

It is seen from Fig. 12(a) that the average temperature in the four cases is a bit different at the same melting fraction. And the average temperature in the case of $H = 0$ mm is the highest at $f_l = 1.0$. That should be attributed to the longest heating time, as Fig. 9(a) indicates. Fig. 12(b) shows that the maximum temperature difference generally decreases with the melting fraction. This is because the highest temperature of energy storage materials is about 75 °C, i.e. the temperature of the inner tube; the lowest temperature increases with the melting fraction. At $f_l = 0.1$ and 0.2, the temperature difference in the case of H

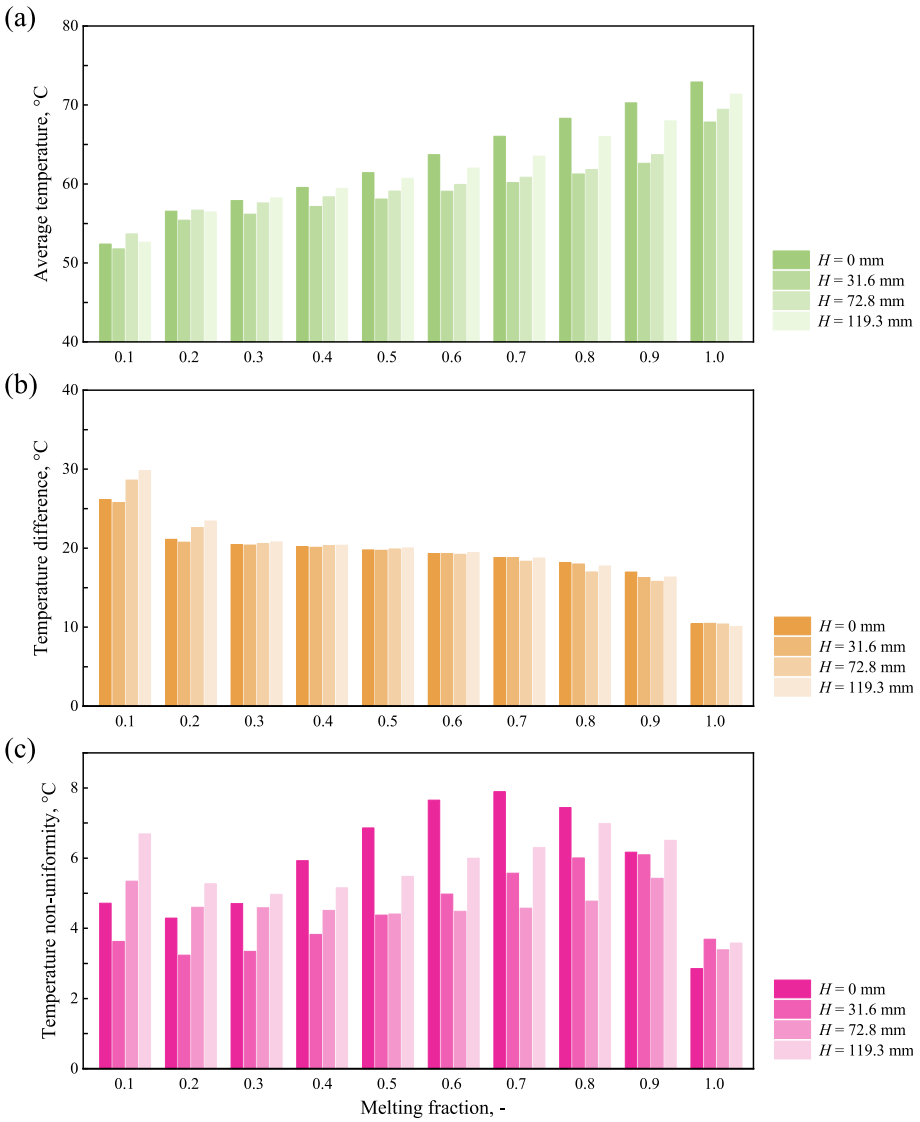

Fig. 12. (a) Average temperature, (b) maximum temperature difference and (c) temperature non-uniformity index in different cases.

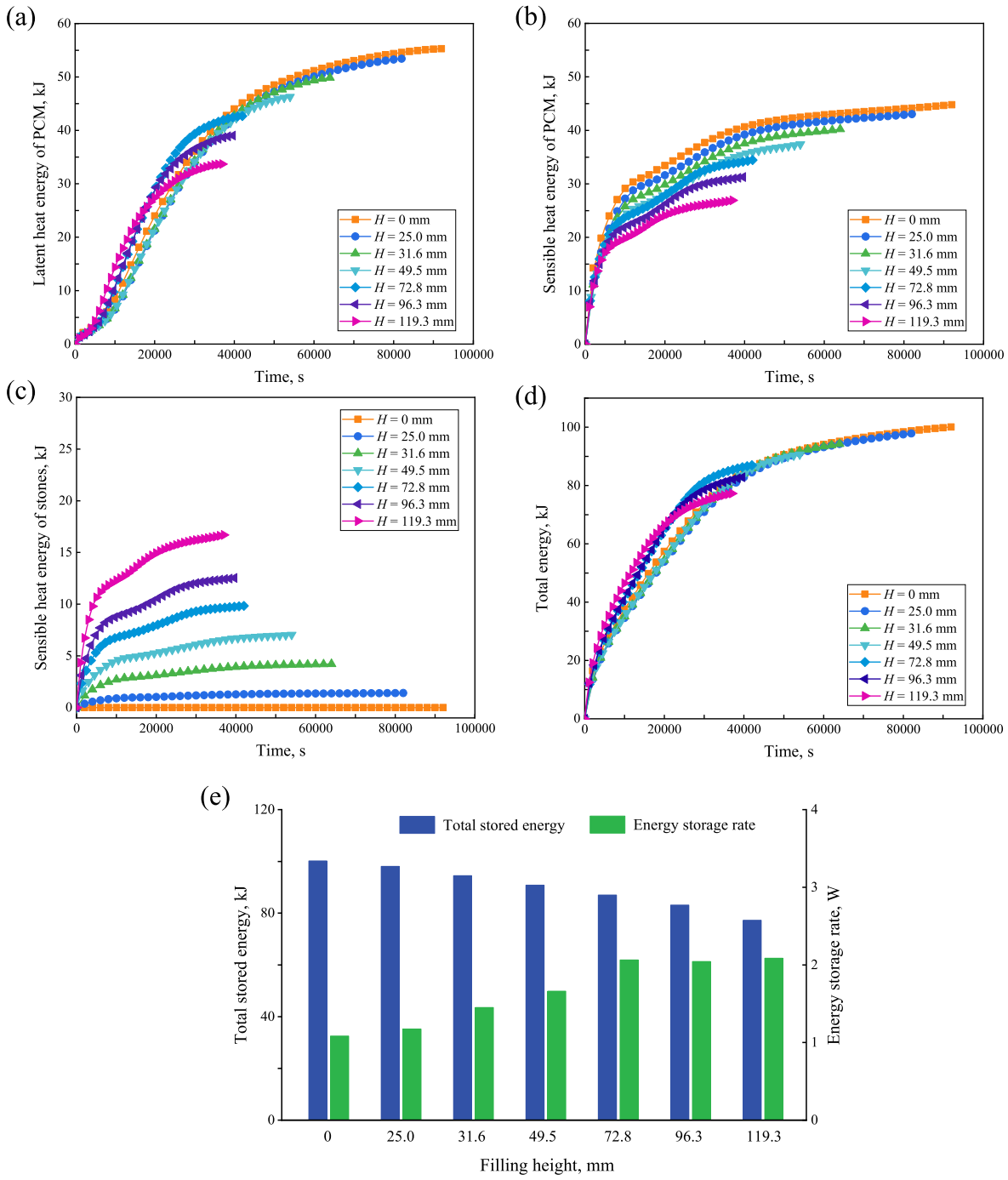

Fig. 13. (a) Variation of the latent heat energy of phase change material with time; (b) variation of the sensible heat energy of phase change material with time; (c) variation of the sensible heat energy of stones; (d) variation of the total energy with time; (e) effect of the filling height on total stored energy and energy storage rate.

= 119.3 mm is the largest; however, afterwards, the four cases have nearly the same temperature difference. Namely, although stones replace some PCM in the heat storage unit, the maximum temperature difference rarely changes. At $f_l = 0.1$ (0.2 and 0.3), the case of $H = 119.3$ mm has the highest non-uniformity index. As the melting proceeds, the temperature non-uniformity index in the case of $H = 0$ mm becomes the highest. It is because the thermal conductivity of the PCM is low, and the amount of the PCM in the case of $H = 0$ mm is the largest, which leads to poor heat transfer performance. However, since the total heating time is the longest, the PCM is heated fully, so the temperature distribution in the case of $H = 0$ mm is the most uniform at $f_l = 1.0$. The difference in the temperature uniformity between cases of $H = 31.6$ mm, $H = 72.8$ mm and $H = 119.3$ mm is insignificant finally.

Fig. 13(a)-(d) shows various energy parameters. It is seen that the variation of latent heat energy is similar to that of melting volume. The sensible heat energy of the PCM in the case of $H = 0$ mm always rises fastest because the amount of the PCM is the most. Fig. 13(c) indicates that the difference in the sensible heat energy of stones between different cases is significant. The case of $H = 119.3$ mm stores sensible heat energy much faster than other cases, not only because the amount of stones is more, but because the temperature increases faster.

It is seen from Fig. 13(d) that the total energy in cases of $H = 25.0$ mm, $H = 31.6$ mm, and $H = 49.5$ mm rises slightly slower than that in the case of $H = 0$ mm, but the average energy storage rate is higher

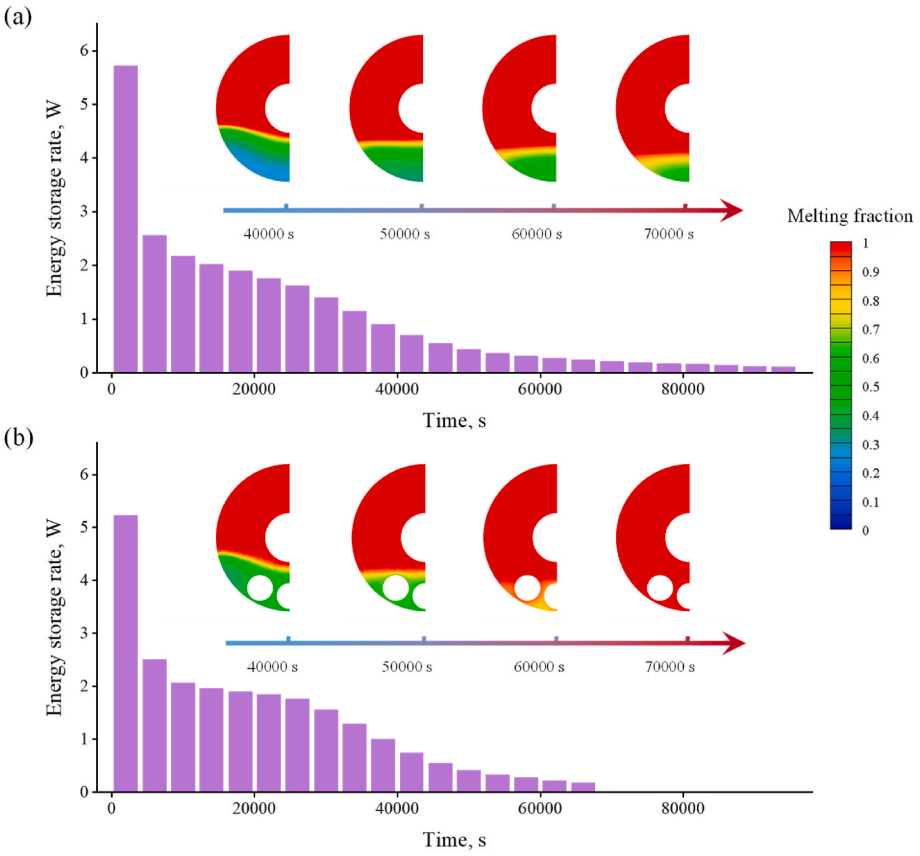

Fig. 14. Energy storage rate and melting front at different time in cases of (a) $H = 0$ mm and (b) $H = 31.6$ mm.

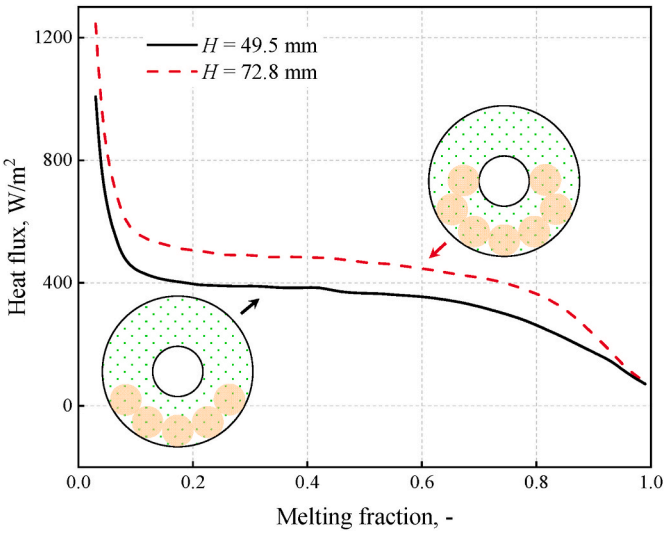

Fig. 15. Heat flux of the inner tube in cases of $H = 49.5$ mm and $H = 72.8$ mm.

(Fig. 13(e)). The average energy storage rate in the case of $H = 25.0$ mm is 8.3% higher than that in the case of $H = 0$ mm. For the case of $H = 0$ mm, the energy storage rate in the final stage is very low (Fig. 14) because heat conduction is the primary heat transfer mode for the bottom PCM. As the thermal conductivity of the PCM is low, it takes quite a long time to melt the bottom PCM. For the case of $H = 31.6$ mm, stones replace some bottom PCM; moreover, their thermal conductivity is higher; thus, the melting time of the bottom PCM is shortened, and the average energy storage rate is improved. As Fig. 14 shows, at 40,000 s, the amount of the liquid PCM in cases of $H = 0$ mm and $H = 31.6$ mm is almost identical. At 70,000 s, there is still some mushy PCM in the case of $H = 0$ mm; by contrast, the PCM is melted fully in the case of $H = 31.6$ mm.

The total energy in the case of $H = 119.3$ mm rises fastest before 20,000 s, and its average energy storage rate is the highest (Fig. 13(e)). And the energy storage rate is increased by 92.6% compared to the case of $H = 0$ mm. The average energy storage rates in cases of $H = 72.8$ mm, $H = 96.3$ mm, and $H = 119.3$ mm are almost identical (2.06 W, 2.04 W, and 2.09 W, respectively). It is noted that the average energy storage rates of the three cases are significantly higher than those of the other cases. That should be attributed to the fact that stones are in contact with the inner tube. The heat flux of the inner tube in cases of $H = 49.5$ mm and $H = 72.8$ mm is plotted in Fig. 15. The melting fraction, rather than time, is used as the x-axis to reduce the influence of temperature difference on heat flux. As shown in Fig. 15, the heat flux in the case of $H = 72.8$ mm is higher than that in the case of $H = 49.5$ mm, indicating stones have better performance in transferring the heat of the inner tube.

Since the total stored energy in the case of $H = 72.8$ mm is more (87.0 kJ, compared to 83.1 kJ in the case of $H = 96.3$ mm, and 77.3 kJ in the case of $H = 119.3$ mm), this case is superior.

3.2. Parametric optimization

The effect of different sizes of stones is analysed to find the superior ones, and the variation of the melting volume of the PCM is plotted in Fig. 16(a). The melting volume (and the stored energy in the following) in all the cases is calculated based on a 40 mm-length heat storage unit. The cases in Fig. 16(a) are under the maximum and minimum void fractions (ε). It is seen that under the minimum void fraction, the PCM in the case of $d = 20$ mm is melted faster, while under the maximum fraction, the PCM in the case of $d = 40$ mm is melted faster. Fig. 16(b)

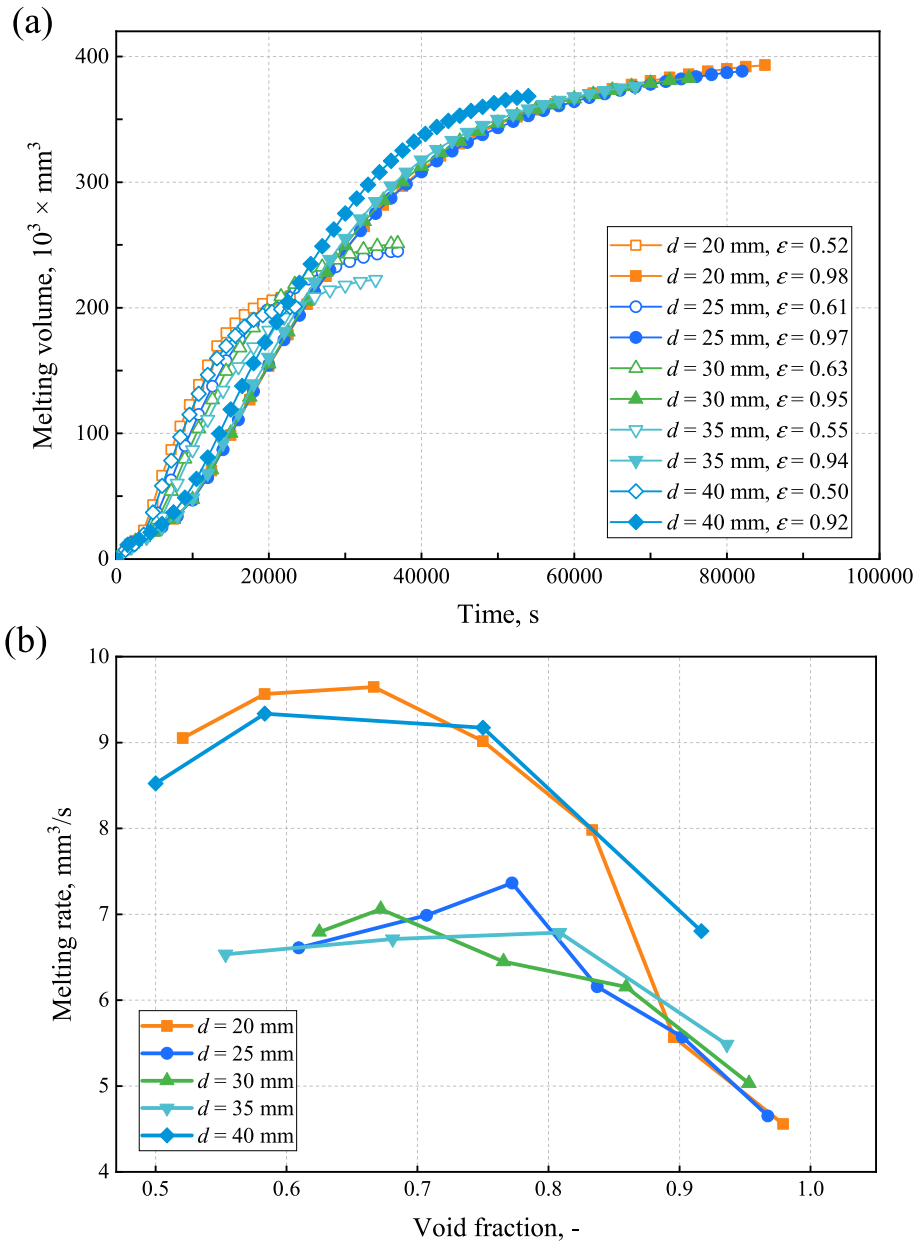

Fig. 16. (a) Variation of melting volume of the PCM enhanced by different sizes of stones at maximum and minimum void fractions; (b) influence of the stone size on melting rate.

indicates that the case of $d = 40$ mm has a much higher average melting rate. The melting rate in the case of $d = 20$ mm is also high when the void fraction is less than 0.89. It is noted that for all sizes of stones, the melting rate first increases with the void fraction and then decreases. There is always a peak melting rate. For example, the peak melting rate occurs at $\varepsilon = 0.67$ in the case of $d = 20$ mm while at $\varepsilon = 0.77$ in the case of $d = 25$ mm.

Fig. 17(a) shows the variation of the stored energy in different cases. Similar to the melting volume, the case of $d = 20$ mm stores thermal energy faster under the minimum void fraction, while the case of $d = 40$ mm stores thermal energy faster under the maximum fraction. However, the size of stones has little influence on the total stored energy that increases almost linearly with the void fraction, as Fig. 17(b) indicates.

As indicated in Fig. 18(a), the energy storage rate is influenced significantly by the stone size, and cases of $d = 20$ mm and $d = 40$ mm generally have a higher energy storage rate. When the void fraction is around 0.6, the energy storage rate in the case of $d = 20$ mm ($\varepsilon = 0.58$) is 3.10 W, while that in the case of $d = 25$ mm ($\varepsilon = 0.61$) is 2.09 W; the former is 48.3% higher than the latter. At the high void fraction ($\varepsilon > 0.89$), the energy storage rate in the case of $d = 20$ mm is low.

The cases of $d = 20$ mm ($\varepsilon = 0.58$) and $d = 25$ mm ($\varepsilon = 0.61$) have a similar void fraction, and their heat flux is plotted in Fig. 18(b). For the case of $d = 20$ mm, more stones surround the inner tube, which is beneficial for transferring the tube's heat. As a result, the heat flux and energy storage rate are higher. The difference in the stone arrangement between these two cases mainly lies in the lower half. As indicated in Fig. 18(c), the number of stones surrounding the lower half of the tube is more than that in the case of $d = 25$ mm, which accelerates the melting of the PCM at the lower half.

4. Conclusions

In the current study, natural stones are used to enhance the heat transfer of the PCM, forming a hybrid sensible-latent heat storage

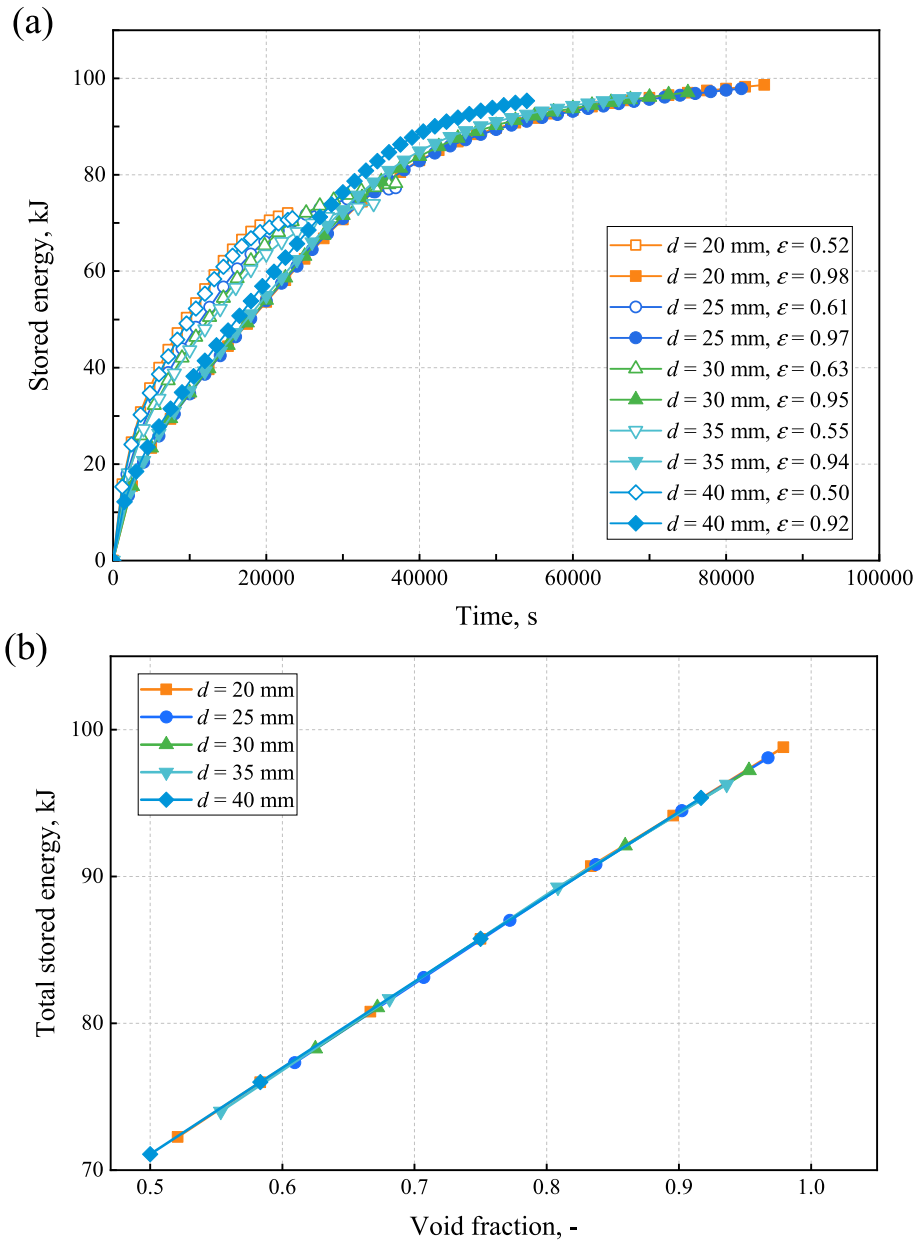

Fig. 17. (a) Variation of the stored energy in cases with different sizes of stones at maximum and minimum void fractions; (b) influence of the stone size on total stored energy.

configuration. Namely, stones not only act as sensible heat storage media but as the thermal enhancer of the PCM. They have the advantages of being widely accessible, low-cost, and environmentally friendly. Melting front, temperature response, and energy storage performance are analysed. The following conclusions are drawn.

(1) The energy storage rate of all 25 mm-stone filling cases is increased. The minimum increase is 8.3%, while the maximum is 92.6%. The case with a filling height of 72.8 mm is superior owing to the high energy storage rate and large total stored energy.
(2) The enhancement mechanism is different according to the filling height. For cases where stones are not in contact with the tube, the energy storage rate is improved by shortening the melting time of the bottom PCM. For cases where stones are in contact with the tube, the energy storage rate is improved by conducting the tube's heat.
(3) The total stored energy, which increases almost linearly with the void fraction, is rarely influenced by the stone size, while the energy storage rate is affected significantly. At the void fraction of about 0.6, the energy storage rate in the case of 20 mm-sized stones is 48.3% higher than that of 25 mm-sized stones. The case with 20 mm or 40 mm-sized stones generally has a higher energy storage rate. Since more stones surround the inner tube, the tube's heat can be transferred better; as a result, the heat flux and energy storage rate are higher.

CRediT authorship contribution statement

Shuai Zhang: Conceptualization, Investigation, Numerical Modelling, Writing – original draft, revision, response to comments. **Yuying Yan:** Conceptualization, Formal analysis, Supervision, Arrange funding, Writing – review & editing, revision, response to comments.

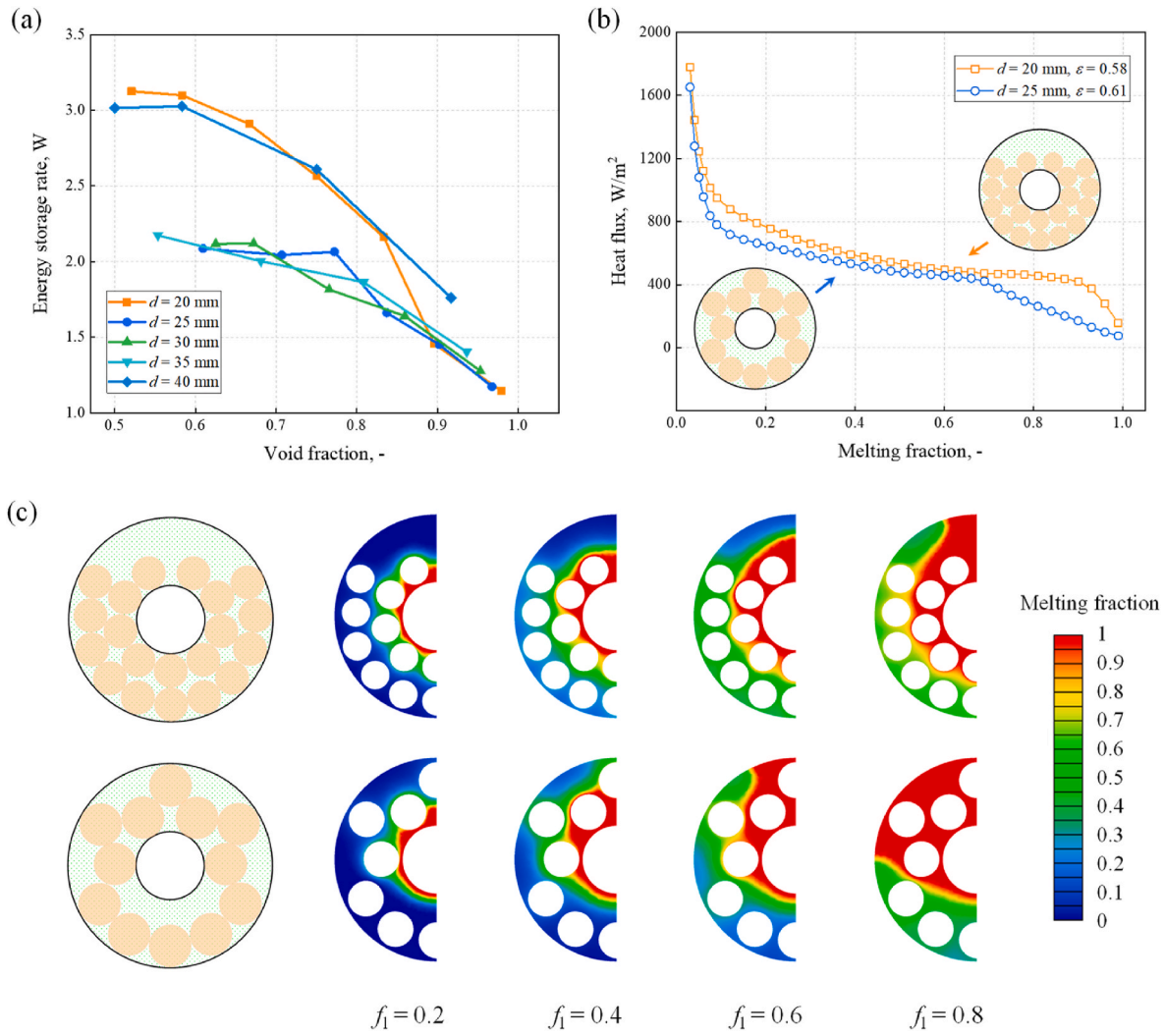

Fig. 18. (a) Effect of the stone size on energy storage rate; (b) heat flux of the inner tube in cases of $d = 20$ mm and $d = 25$ mm; (c) melting front in cases of $d = 20$ mm ($\varepsilon = 0.58$) and $d = 25$ mm ($\varepsilon = 0.61$) under different average melting fractions (the plane at half the thickness).

Declaration of competing interest

The authors declare that they have no known competing financial interests or personal relationships that could have appeared to influence the work reported in this paper.

Acknowledgements

We would like to thank H2020-MSCA-RISE-778104–ThermaSMART and doctoral degree scholarship of China Scholarship Council (CSC).

Nomenclature

HTF	Heat transfer fluid
PCM	Phase change material
SHM	Sensible heat storage material
TES	Thermal energy storage
A_{mushy}	Mushy zone constant, kg/(m^3·s)
c_p	Specific heat capacity, J/(kg·K)
d	Diameter of stones, mm
D_{tube}, D_{shell}	Tube diameter and shell diameter, mm
f_l	Average melting fraction
g	Gravitational acceleration, m/s^2
H	Filling height of stones, mm
k	Thermal conductivity, W/(m·K)
l_u	Length of a single unit, mm
L	Latent heat, J/kg
n	Number of cells

$\boldsymbol{n}$	Unit normal vector
N	Number of stones in a single unit
p	Pressure, Pa
t	Time, s
T	Temperature, K
T_0	Initial temperature, °C
T_i (f_l)	Temperature of cell i at f_l, K
$T_{m,s}$, $T_{m,l}$	Solidus temperature and liquidus temperature of PCM, K
ΔT	Maximum temperature difference, °C
$\overline{T(f_l)}$	Average temperature at f_l, K
u, v, w	Velocity in x, y and z direction, m/s
U	Fluid velocity, m/s
V	Volume, m^3

Greek letters

ρ	Density, kg/m^3
μ	Viscosity, Pa·s
ω	A small number
β	Thermal expansion coefficient, K^{-1}
δ	Temperature non-uniformity index, °C
ε	Void fraction
φ	Melting fraction in the cell

Subscripts

max	Maximum
min	Minimum
PCM	Phase change material

References

[1] S. Zhang, Z. Li, Y. Yao, L. Tian, Y. Yan, Heat transfer characteristics and compatibility of molten salt/ceramic porous composite phase change material, Nano Energy 100 (2022), 107476.

[2] J. Ding, G. Pan, L. Du, J. Lu, X. Wei, J. Li, W. Wang, J. Yan, Theoretical prediction of the local structures and transport properties of binary alkali chloride salts for concentrating solar power, Nano Energy 39 (2017) 380–389.

[3] G. Alva, L. Liu, X. Huang, G. Fang, Thermal energy storage materials and systems for solar energy applications, Renew. Sustain. Energy Rev. 68 (2017) 693–706.

[4] S. Kuravi, J. Trahan, D.Y. Goswami, M.M. Rahman, E.K. Stefanakos, Thermal energy storage technologies and systems for concentrating solar power plants, Prog. Energy Combust. Sci. 39 (2013) 285–319.

[5] S. Zhang, Y. Yan, Thermal performance of latent heat energy storage system with/without enhancement under solar fluctuation for Organic Rankine power cycle, Energy Convers. Manag. 270 (2022), 116276.

[6] J. Yang, J. Li, Z. Yang, Y. Duan, Thermodynamic analysis and optimization of a solar organic Rankine cycle operating with stable output, Energy Convers. Manag. 187 (2019) 459–471.

[7] H. Yu, H. Helland, X. Yu, T. Gundersen, G. Sin, Optimal design and operation of an Organic Rankine Cycle (ORC) system driven by solar energy with sensible thermal energy storage, Energy Convers. Manag. 244 (2021), 114494.

[8] S. Zhang, D. Feng, L. Shi, L. Wang, Y. Jin, L. Tian, Z. Li, G. Wang, L. Zhao, Y. Yan, A review of phase change heat transfer in shape-stabilized phase change materials (ss-PCMs) based on porous supports for thermal energy storage, Renew. Sustain. Energy Rev. 135 (2021), 110127.

[9] H. Zhang, J. Baeyens, G. Cáceres, J. Degreve, Y. Lv, Thermal energy storage: recent developments and practical aspects, Prog. Energy Combust. Sci. 53 (2016) 1–40.

[10] A. Gil, M. Medrano, I. Martorell, A. Lázaro, P. Dolado, B. Zalba, L.F. Cabeza, State of the art on high temperature thermal energy storage for power generation. Part 1—concepts, materials and modellization, Renew. Sustain. Energy Rev. 14 (2010) 31–55.

[11] A. Gautam, R.P. Saini, A review on sensible heat based packed bed solar thermal energy storage system for low temperature applications, Sol. Energy 207 (2020) 937–956.

[12] G. Alva, Y. Lin, G. Fang, An overview of thermal energy storage systems, Energy 144 (2018) 341–378.

[13] S. Zhang, Y. Yan, Energy, exergy and economic analysis of ceramic foam-enhanced molten salt as phase change material for medium- and high-temperature thermal energy storage, Energy 262 (2023), 125462.

[14] N.I. Ibrahim, F.A. Al-Sulaiman, S. Rahman, B.S. Yilbas, A.Z. Sahin, Heat transfer enhancement of phase change materials for thermal energy storage applications: a critical review, Renew. Sustain. Energy Rev. 74 (2017) 26–50.

[15] J. Guo, Z. Liu, Z. Du, J. Yu, X. Yang, J. Yan, Effect of fin-metal foam structure on thermal energy storage: an experimental study, Renew. Energy 172 (2021) 57–70.

[16] S. Zhang, Y. Yao, Y. Jin, Z. Shang, Y. Yan, Heat transfer characteristics of ceramic foam/molten salt composite phase change material (CPCM) for medium-temperature thermal energy storage, Int. J. Heat Mass Tran. 196 (2022), 123262.

[17] P. Zhang, Z.N. Meng, H. Zhu, Y.L. Wang, S.P. Peng, Melting heat transfer characteristics of a composite phase change material fabricated by paraffin and metal foam, Appl. Energy 185 (2017) 1971–1983.

[18] Z. Liu, Y. Yao, H. Wu, Numerical modeling for solid–liquid phase change phenomena in porous media: shell-and-tube type latent heat thermal energy storage, Appl. Energy 112 (2013) 1222–1232.

[19] B. Buonomo, O. Manca, S. Nardini, R.E. Plomitallo, Numerical study on latent heat thermal energy storage system with PCM partially filled with aluminum foam in local thermal equilibrium, Renew. Energy 195 (2022) 1368–1380.

[20] S. Zhang, Y. Yan, Evaluation of discharging performance of molten salt/ceramic foam composite phase change material in a shell-and-tube latent heat thermal energy storage unit, Renew. Energy 198 (2022) 1210–1223.

[21] X. Yang, Z. Lu, Q. Bai, Q. Zhang, L. Jin, J. Yan, Thermal performance of a shell-and-tube latent heat thermal energy storage unit: role of annular fins, Appl. Energy 202 (2017) 558–570.

[22] Y. Huang, X. Liu, Charging and discharging enhancement of a vertical latent heat storage unit by fractal tree-shaped fins, Renew. Energy 174 (2021) 199–217.

[23] M.A. Dekhil, J.V. Simo Tala, O. Bulliard-Sauret, D. Bougeard, Numerical analysis of the performance enhancement of a latent heat storage shell and tube unit using finned tubes during melting and solidification, Appl. Therm. Eng. 192 (2021), 116866.

[24] J.M. Mahdi, H.I. Mohammed, E.T. Hashim, P. Talebizadehsardari, E.C. Nsofor, Solidification enhancement with multiple PCMs, cascaded metal foam and nanoparticles in the shell-and-tube energy storage system, Appl. Energy 257 (2020), 113993.

[25] M. Parsazadeh, X. Duan, Numerical study on the effects of fins and nanoparticles in a shell and tube phase change thermal energy storage unit, Appl. Energy 216 (2018) 142–156.

[26] H. Shabgard, T.L. Bergman, N. Sharifi, A. Faghri, High temperature latent heat thermal energy storage using heat pipes, Int. J. Heat Mass Tran. 53 (2010) 2979–2988.

[27] K. Nithyanandam, R. Pitchumani, Computational studies on a latent thermal energy storage system with integral heat pipes for concentrating solar power, Appl. Energy 103 (2013) 400–415.

[28] Z. Duan, Z. Zhang, J. Wang, X. Cao, J. Zhang, Thermal performance of structured packed bed with encapsulated phase change materials, Int. J. Heat Mass Tran. 158 (2020), 120066.

[29] W.-J. Luo, P. Vishwakarma, B. Panigrahi, Hydrodynamic influence on thermal management of flexible heatsink devices embedded with out-of-plane intricate microchannel design, Int. Commun. Heat Mass Tran. 144 (2023), 106792.

[30] J. Yang, L. Yang, C. Xu, X. Du, Numerical analysis on thermal behavior of solid–liquid phase change within copper foam with varying porosity, Int. J. Heat Mass Tran. 84 (2015) 1008–1018.

[31] R. Ge, Q. Li, C. Li, Q. Liu, Evaluation of different melting performance enhancement structures in a shell-and-tube latent heat thermal energy storage system, Renew. Energy 187 (2022) 829–843.
[32] L. Pu, S. Zhang, L. Xu, Z. Ma, X. Wang, Numerical study on the performance of shell-and-tube thermal energy storage using multiple PCMs and gradient copper foam, Renew. Energy 174 (2021) 573–589.
[33] Y. Yao, H. Wu, Macroscale modeling of solid–liquid phase change in metal foam/paraffin composite: effects of paraffin density treatment, thermal dispersion, and interstitial heat transfer, J. Therm. Sci. Eng. Appl. (2021) 13.
[34] J.M. Mahdi, E.C. Nsofor, Solidification enhancement in a triplex-tube latent heat energy storage system using nanoparticles-metal foam combination, Energy 126 (2017) 501–512.
[35] Ansys Help, The Boussinesq Model, 2023. https://ansyshelp.ansys.com/account/secured?returnurl=/Views/Secured/corp/v211/en/flu_ug/flu_ug_sec_hxfer_buoy.html?q=Boussinesq.
[36] Y. Huang, Z. Deng, Y. Chen, C. Zhang, Performance investigation of a biomimetic latent heat thermal energy storage device for waste heat recovery in data centers, Appl. Energy 335 (2023), 120745.
[37] Y. Yao, H. Wu, Z. Liu, Direct simulation of interstitial heat transfer coefficient between paraffin and high porosity open-cell metal foam, J. Heat Tran. 140 (2018), 032601.
[38] S. Zhang, Z. Li, H. Wang, L. Tian, Y. Jin, M. Alston, Y. Yan, Component-dependent Thermal Properties of Molten Salt Eutectics for Solar Thermal Energy Storage: Experiments, Molecular Simulation and Applications, Applied Thermal Engineering, 2022, 118333.
[39] M. Caliano, N. Bianco, G. Graditi, L. Mongibello, Analysis of a phase change material-based unit and of an aluminum foam/phase change material composite-based unit for cold thermal energy storage by numerical simulation, Appl. Energy 256 (2019), 113921.
[40] A. Atal, Y. Wang, M. Harsha, S. Sengupta, Effect of porosity of conducting matrix on a phase change energy storage device, Int. J. Heat Mass Tran. 93 (2016) 9–16.
[41] A.A. Al-Abidi, S. Mat, K. Sopian, M.Y. Sulaiman, A.T. Mohammad, Numerical study of PCM solidification in a triplex tube heat exchanger with internal and external fins, Int. J. Heat Mass Tran. 61 (2013) 684–695.